

# Determination of the $^{142}\text{Ce}(\gamma, n)$ cross section using quasi-monoenergetic Compton backscattered $\gamma$ rays

A. Sauerwein,<sup>1,\*</sup> K. Sonnabend,<sup>1</sup> M. Fritzsche,<sup>2</sup> J. Glorius,<sup>1</sup> E. Kwan,<sup>3,4,†</sup> N. Pietralla,<sup>2</sup> C. Romig,<sup>2</sup> G. Rusev,<sup>3,4,‡</sup> D. Savran,<sup>5,6</sup> L. Schnorrenberger,<sup>2</sup> A. P. Tonchev,<sup>3,4,§</sup> W. Tornow,<sup>3,4</sup> and H. R. Weller<sup>3,4</sup>

<sup>1</sup>*Institut für Angewandte Physik, Goethe Universität Frankfurt am Main, D-60438 Frankfurt am Main, Germany*

<sup>2</sup>*Institut für Kernphysik, Technische Universität Darmstadt, D-64289 Darmstadt, Germany*

<sup>3</sup>*Department of Physics, Duke University, Durham, North Carolina 27708, USA*

<sup>4</sup>*Triangle Universities Nuclear Laboratory (TUNL), Durham, North Carolina 27708, USA*

<sup>5</sup>*ExtreMe Matter Institute EMMI and Research Division, GSI Helmholtzzentrum für Schwerionenforschung, GmbH, D-64291 Darmstadt, Germany*

<sup>6</sup>*Frankfurt Institute for Advanced Studies FIAS, D-60438 Frankfurt am Main, Germany*

(Received 2 January 2014; published 7 March 2014)

**Background:** Knowing the energy dependence of the  $(\gamma, n)$  cross section is mandatory to predict the abundances of heavy elements using astrophysical models. The data can be applied directly or used to constrain the cross section of the inverse  $(n, \gamma)$  reaction.

**Purpose:** The measurement of the reaction  $^{142}\text{Ce}(\gamma, n)^{141}\text{Ce}$  just above the reaction threshold amends the existing experimental database in that mass region for  $p$ -process nucleosynthesis and helps to understand the  $s$ -process branching at the isotope  $^{141}\text{Ce}$ .

**Method:** The quasi-monoenergetic photon beam of the High Intensity  $\gamma$ -ray Source (HI $\gamma$ S), TUNL, USA, is used to irradiate naturally composed Ce targets. The reaction yield is determined afterwards with high-resolution  $\gamma$ -ray spectroscopy.

**Results:** The experimental data are in agreement with previous measurements at higher energies. Since the cross-section prediction of the  $^{142}\text{Ce}(\gamma, n)$  reaction is exclusively sensitive to the  $\gamma$ -ray strength function, the resulting cross-section values were compared to Hauser-Feshbach calculations using different  $\gamma$ -ray strength functions. A microscopic description within the framework of the Hartree-Fock-BCS model describes the experimental values well within the measured energy range.

**Conclusions:** The measured data show that the predicted  $(\gamma, n)$  reaction rate is correct within a factor of 2 even though the closed neutron shell  $N = 82$  is approached. This agreement allows us to constrain the  $(n, \gamma)$  cross section and to improve the understanding of the  $s$ -process branching at  $^{141}\text{Ce}$ .

DOI: [10.1103/PhysRevC.89.035803](https://doi.org/10.1103/PhysRevC.89.035803)

PACS number(s): 25.20.Dc, 24.60.Dr, 26.30.-k

## I. INTRODUCTION

The elements heavier than iron are mainly produced via two neutron capture processes: the slow neutron capture process ( $s$  process) and the rapid neutron capture process ( $r$  process). The  $s$  process takes place under moderate neutron density of roughly  $10^7$  neutrons per  $\text{cm}^3$ . The time scale between two subsequent neutron capture reactions is then typically of the order of years [1]. The  $s$ -process path propagates along the valley of stability. Whenever an unstable nucleus is reached with a half-life of the same order of magnitude as the average time for a second neutron capture process, the reaction path branches. The nuclear properties of these branching-point nuclei are of particular interest, since they influence the isotopic abundance distribution of the neighboring elements [2].

In contrast to the  $s$  process, the  $r$  process acts at higher neutron densities in excess of  $10^{20} \text{ cm}^{-3}$ . This high neutron flux leads to the production of very neutron-rich nuclei about 20 mass units away from the valley of stability [3]. During the so-called freeze-out, the produced unstable nuclei decay back to the valley of stability [4].

However, there are about 35 neutron-deficient nuclei that cannot be produced via neutron-capture reactions [5]. According to current knowledge, many processes contribute to the production of these so-called  $p$  nuclei [6]. One of these processes, the  $\gamma$  process, proceeds at extremely high temperatures of 2 GK to 3 GK. Hence, photodisintegration reactions, i.e.,  $(\gamma, n)$ ,  $(\gamma, p)$ , and  $(\gamma, \alpha)$  reactions, on heavy seed nuclei previously produced in the  $s$  and  $r$  processes play a dominant role in the  $\gamma$  process [7,8].

In total, these nucleosynthesis processes include several thousand reactions on mostly unstable nuclei. Therefore, most reaction rates cannot be measured and must be calculated using theoretical models. Reaction rates for nuclides heavier than calcium are mainly adopted by Hauser-Feshbach statistical-model calculations [9,10]. While the statistical model is well established, major uncertainties stem from various nuclear physics models entering the calculations. Those nuclear physics models include, besides others, descriptions of the

\*sauerwein@iap.uni-frankfurt.de

<sup>†</sup>Present address: National Superconducting Cyclotron Laboratory, Michigan State University, East Lansing, Michigan 48824, USA.

<sup>‡</sup>Present address: Chemistry Division, Los Alamos National Laboratory, Los Alamos, New Mexico 87545, USA.

<sup>§</sup>Present address: Physics Division, Lawrence Livermore National Laboratory, Livermore, California 94550, USA.

nuclear level densities,  $\gamma$ -ray strength functions, and optical-model potentials. In order to enhance the reliability of these predictions, experimental data are required.

The investigation of the photodisintegration reaction  $^{142}\text{Ce}(\gamma, n)^{141}\text{Ce}$  is interesting for two reasons. First, the nucleus  $^{141}\text{Ce}$  acts as a branching point nucleus in the  $s$ -process path. Its neutron-capture cross section determines the abundance ratio of the isotopes  $^{141}\text{Pr}$  and  $^{142}\text{Nd}$  relative to  $^{142}\text{Ce}$ . The experimental results for the  $^{142}\text{Ce}(\gamma, n)$  ground-state cross section can verify the integral reliability of the statistical-model predictions. Second, a considerable number of photodisintegration reactions takes place during the  $\gamma$  process. Systematic studies of  $(\gamma, n)$  reactions were performed recently [11–21] in order to check the reliability of the cross-section predictions for the ground-state contribution, even though reactions on excited states play an important role in the stellar plasma [22]. The data of this work enlarge this experimental database.

Additionally,  $^{142}\text{Ce}$  is near the  $N = 82$  neutron shell closure, where some of the assumptions involved in the statistical-model calculations, e.g., a sufficiently high level density for a statistical treatment, are often not entirely fulfilled. Therefore, it is interesting to investigate whether any significant deviation between experiment and theory can be observed when the neutron magic number is approached.

In Sec. II, we describe our experimental setup while Sec. III explains the analysis of the data. Finally, the experimental results are presented and compared to calculations using different  $\gamma$ -ray strength functions in Sec. IV.

## II. EXPERIMENT

The cross section of the photon-neutron reaction on  $^{142}\text{Ce}$  was measured at the High Intensity  $\gamma$ -ray Source (HI $\gamma$ S) at Triangle Universities Nuclear Laboratory (Durham, NC, USA) in the excitation energy region just above the neutron separation energy  $S_n$  between 7.6 and 9.7 MeV using the activation technique. The determination of the absolute photon intensity was derived from a normalization to the  $^{187}\text{Re}(\gamma, n)$  reaction [23].

### A. Preparation of the targets

Eight target samples were prepared for this experiment from naturally composed  $\text{CeO}_2$  powder at the Karlsruhe Institute of Technology. To enhance the stability of the targets, the  $\text{CeO}_2$  powder was mixed with a well-defined amount of pure graphite powder. This mixture was then pressed into thin disks, 20 mm in diameter, and masses between 780 and 940 mg each, corresponding to a mass of pure cerium dioxide between 660 and 740 mg. In order to avoid losses of target material, the target disks were covered by mylar foils. The normalization standards consisted of metallic foils of naturally composed rhenium that were disks also of 20 mm diameter and had masses between 320 and 340 mg.

### B. Experimental installation at TUNL

Intracavity backscattering of free-electron laser (FEL) photons is utilized at HI $\gamma$ S in order to produce fully polarized

$\gamma$ -ray beams. Gamma-ray beams with photon energies of up to 100 MeV and total intensities in excess of  $10^8$   $\gamma$  rays per second can be produced [24]. HI $\gamma$ S consists of a 280-MeV linac preinjector; a top-off, full-energy booster injector; and a 1.2-GeV electron storage ring. The HI $\gamma$ S  $\gamma$ -ray beam is generated in the middle of a long straight section of the storage ring by colliding the electron beam with a FEL beam produced by the same electron beam. A passive collimator system at a distance of about 60 m from the collision point determines the intensity and the energy resolution of the  $\gamma$ -ray beam delivered to the experiment. A careful adjustment of the collimator to the experimental needs is mandatory. Further information about this facility can be found in Ref. [24].

To produce sufficient activity within the rather short time of irradiation, a collimator diameter of 2.54 cm was chosen. This allows us to irradiate the complete target material so deviations in the target thickness can be neglected in the analysis. However, this also results in a rather broad energy distribution of the photons with a full width at half maximum (FWHM) of about 5% compared to the energy with maximum intensity.

### C. Irradiation and $\gamma$ counting

The irradiations of natural cerium dioxide samples were carried out in an experiment together with the irradiation of zirconium samples. The experimental results on  $^{96}\text{Zr}(\gamma, n)$  will be published separately. Furthermore, nuclear structure experiments were simultaneously carried out further downstream using the same photon beam [25,26].

The targets were irradiated with laser Compton backscattered  $\gamma$  rays at energies between 7.6 MeV and 9.7 MeV. The  $\gamma$ -beam energies are given in Table III. They are all above the neutron emission threshold of  $^{142}\text{Ce}$ , while only the two highest are above the neutron emission threshold of the neutron-magic isotope  $^{140}\text{Ce}$  as can be seen from Table I. Two rhenium samples were irradiated together with the targets of interest at each activation energy. The cerium targets were sandwiched between these rhenium samples in order to determine the absolute value of the photon flux. Details about this part of the analysis can be found in Sec. IIIB.

The irradiations typically took between 2 and 4.5 h. The activity of the target samples after irradiation was determined in a separate counting setup under low-background

TABLE I. Isotopic abundances  $I_{\%}$  and neutron separation energies  $S_n$  for cerium isotopes and for  $^{187}\text{Re}$ , which was used for the determination of the absolute value of the photon flux during the irradiation. For details about this procedure see text. The isotopic abundances are taken from Ref. [27] and neutron separation energies are taken from Ref. [28].

Isotope	$I_{\%}(\%)$	$S_n$ (keV)
$^{136}\text{Ce}$	$0.19 \pm 0.01$	$9963.55 \pm 10.27$
$^{138}\text{Ce}$	$0.25 \pm 0.01$	$9721.25 \pm 9.89$
$^{140}\text{Ce}$	$88.48 \pm 0.10$	$9200.29 \pm 7.18$
$^{142}\text{Ce}$	$11.08 \pm 0.10$	$7168.05 \pm 2.42$
$^{187}\text{Re}$	$62.60 \pm 0.02$	$7359.21 \pm 1.07$

TABLE II. Spectroscopy information of  $^{141}\text{Ce}$  and  $^{186}\text{Re}$ . The half-lives  $T_{1/2}$ ,  $\gamma$ -ray energies  $E_\gamma$ , and  $\gamma$ -ray intensities  $I_\gamma$  per radioactive decay are taken from the National Nuclear Data Center [29].

Parent nucleus	$T_{1/2}$ (d)	$E_\gamma$ (keV)	$I_\gamma$ (%)
$^{141}\text{Ce}$	$32.508 \pm 0.013$	$145.433 \pm 0.0014$	$48.29 \pm 0.2$
$^{186}\text{Re}$	$3.7183 \pm 0.0011$	$137.157 \pm 0.008$	$9.47 \pm 0.03$
		$122.64 \pm 0.02$	$0.603 \pm 0.0025$

conditions. The relevant spectroscopy information of the measured nucleus  $^{141}\text{Ce}$  and the monitor nucleus  $^{186}\text{Re}$  is given in Table II. We made use of two HPGe detector setups to measure the  $\gamma$ -ray transitions following  $\beta$  decay of the irradiated samples. One detector setup consisted of a single coaxial HPGe detector with 60% efficiency relative to a 3 inch  $\times$  3 inch NaI detector. This setup is located at TUNL and will be referred to as the HPGe setup. The distance between target and detector was 3 cm. In the second setup, located at Technische Universität Darmstadt, referred to as the LEPS setup, two HPGe low-energy photon spectrometers (LEPS) of almost identical design were used. These detectors were positioned face-to-face having a distance of only 10 mm from each other. Both setups were shielded against naturally occurring background by thick layers of lead and additionally by an inner layer of copper to reduce x-rays and low-energy  $\gamma$  rays stemming from the outer lead layer.

In order to determine the absolute detection efficiency of the LEPS setup, the efficiency of the detectors was simulated in detail using the Monte Carlo code GEANT4 [30]. Additionally, the efficiencies were measured using various calibration sources, which served as normalization for the simulated efficiencies. In a next step, the target geometry and  $\gamma$ -ray absorption were taken into account in the simulation.

The energy dependence of the efficiency of the HPGe setup was also determined using a set of calibration sources. The absolute value was derived from a normalization to the LEPS setup using the same target at both setups.

### III. DATA ANALYSIS

The photoneutron reaction yield  $N_{\text{prod}}$ , i.e., the number of  $^{142}\text{Ce}(\gamma, n)$  reactions induced during the irradiation, was determined from the activity of the irradiated cerium dioxide targets. Hence, the  $\gamma$  rays that are emitted after the radioactive decays of the unstable reaction products are detected offline with a low-background counting setup. The number of detected full-energy events  $C(E_\gamma)$  of a certain transition during the counting time  $t_{\text{meas}}$  is connected with the photoneutron reaction yield  $N_{\text{prod}}$  as follows:

$$N_{\text{prod}} = \frac{C(E_\gamma)}{I_\gamma(E_\gamma)\varepsilon(E_\gamma)\tau}, \quad (1)$$

with

$$\tau = \frac{t_{\text{LIFE}}}{t_{\text{REAL}}} f_{\text{act}} f_{\text{wait}} f_{\text{meas}}. \quad (2)$$

Here,  $I_\gamma(E_\gamma)$  denotes the  $\gamma$ -intensity per radioactive decay and  $\varepsilon(E_\gamma)$  the full-energy peak efficiency of the counting setup. As described in Sec. II C, the full-energy peak efficiency is corrected for  $\gamma$ -ray absorption and for the extended target geometry. The time factors  $t_{\text{LIFE}}/t_{\text{REAL}}$ ,  $f_{\text{act}}$ ,  $f_{\text{wait}}$ , and  $f_{\text{meas}}$  correct for the dead time of the data acquisition, decays of the reaction products during the time of irradiation, during the waiting time between activation and measurement, and during the time of spectroscopy, respectively. Except the dead-time correction  $t_{\text{LIFE}}/t_{\text{REAL}}$ , the time factors are given for a constant photon intensity during the irradiations by the decay law:

$$f_{\text{act}} = \frac{1 - \exp(-\lambda\Delta t_{\text{act}})}{\lambda\Delta t_{\text{act}}}, \quad (3)$$

$$f_{\text{wait}} = \exp(-\lambda\Delta t_{\text{wait}}), \quad (4)$$

and

$$f_{\text{meas}} = 1 - \exp(-\lambda\Delta t_{\text{meas}}). \quad (5)$$

The photon intensity during irradiation was measured quantitatively. A constant intensity was assumed in small time intervals of 60 s.

The photoneutron reaction yield is given by

$$N_{\text{prod}} = N_{\text{target}} \int_0^\infty \sigma(E) N_\gamma(E) dE \quad (6)$$

$$\approx N_{\text{target}} \sigma_0 \int_{S_n}^{E_{\text{max}}} N_\gamma(E) dE. \quad (7)$$

The number of target nuclei is denoted as  $N_{\text{target}}$ , whereas the photoneutron cross section is denoted as  $\sigma(E)$ . The maximum photon energy,  $E_{\text{max}}$ , is indicated in Fig. 1. Due to the narrow energy distribution of the photon beam,  $\sigma(E)$  can be

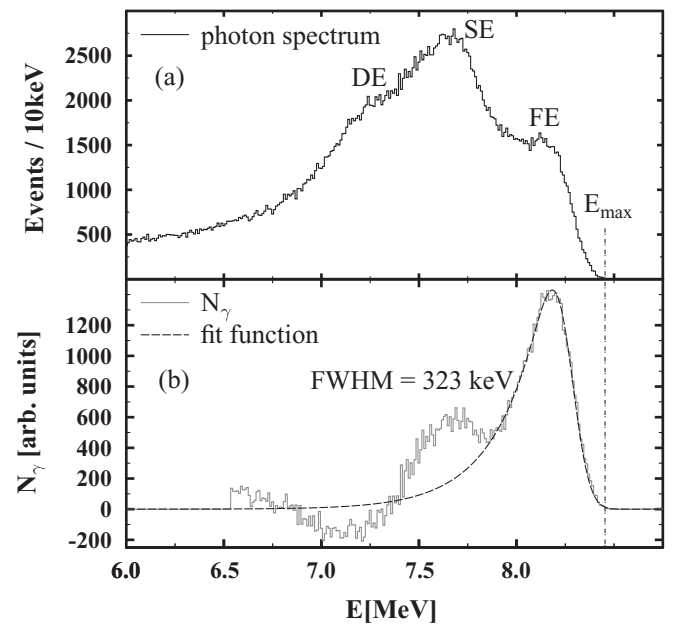


FIG. 1. (a) Photon flux measured at  $0^\circ$  with respect to the beam axis. (b) Photon flux  $N_\gamma$  obtained from deconvolution of the spectrum (histogram). The dashed curve is a function fitted to the histogram as described in the text.

approximated by a constant value  $\sigma_0$  within the interval  $S_n$  to  $E_{\max}$ . The absolute photon flux is given by  $N_\gamma(E)$ .

### A. Deconvolution of the photon flux

In order to determine the reaction yields, the absolute photon flux is needed. That means the spectral distribution and the intensity of the photon flux have to be determined. As described in the following section, the absolute intensity of the photon flux can be obtained using a reference target. In this subsection, the determination of the spectral distribution of the photons is illustrated.

In order to determine the beam energy before each activation run, the spectrum of the incident photons was measured with a HPGe detector at zero degree relative to the beam line using a reduced photon beam intensity.

During each activation, the spectrum of the photons was checked online for changes in the intensity and the distribution of the photons. For this purpose, incoming photons were Compton scattered off a thick copper target, which was installed behind the samples. The HPGe detector was rotated by  $11^\circ$  out of the direct beam to detect the scattered photons. The spectral shape of the photon flux stayed constant over all activation runs, and only small fluctuations in the intensity over time were observed. These small fluctuations were corrected in the data analysis.

The spectra obtained with the detector at  $0^\circ$  to the beam axis were used for the deconvolution of the spectral distribution of the photons. A typical spectrum of photons at  $0^\circ$  is depicted in Fig. 1(a). The expected detector response to a quasi-monoenergetic photon beam is visible. Besides the broad full-energy peak (FE) at 8150 keV, the single-escape peak (SE) and the double-escape peak (DE) are visible at 511 and 1022 keV below the FE peak.

In order to deconvolute the detector response of the photon spectrum, the detector response to monoenergetic photons was simulated with GEANT4 up to the highest energy detected in the photon spectra. Monoenergetic photons were simulated to be emitted from a circular area with a diameter of 2.54 cm, which is the diameter of the collimator for the  $\gamma$ -ray beam. Fifty million photons were considered in each simulation. A bin width of 10 keV was used to compare the simulation to the measured photon spectrum. The full-energy peak of the simulation is normalized to the amount of counts in the channel with the highest energy of the measured photon spectrum. The simulated spectra for each energy are then subtracted one after another using the same normalization process as described for the first channel. This method was described as *spectrum strip method* in Ref. [31]. The deconvoluted photon flux is the sum of the normalized simulated full-energy peaks and is depicted in Fig. 1(b) as a histogram. Besides the expected peak at the full energy, a second peak occurs at the energy of the corresponding single-escape peak, because the simulations underestimate the single-escape peak. These artifacts are not a part of the photon flux. Therefore, a Gaussian function with a tail towards smaller energies was fitted to the photon flux. A boundary condition was used for this fit: At a distance of 511 keV a second peak has to be fitted with the same FWHM

and the same tail. The fitted function, shown in Fig. 1(b) as dashed curve, is used for the analysis.

The method described can be compared to an approach published in Ref. [32], where extensive simulations tuned to the experimental situation were used to avoid the residuals of SE and DE peaks and to yield the absolute value of the photon flux simultaneously. Using that method did not change our results within the uncertainties.

In addition, the shape of the photon flux can also be compared to results of the  $(\gamma, \gamma')$  experiments carried out in parallel [25,26]. Again, no significant deviation to the photon flux obtained by us was observed. Thus, the method presented here is a sufficient approach to determine the spectral distribution of the photon flux.

### B. Absolute value of the photon flux

To determine the absolute integrated photon flux, the target was sandwiched between two normalization standards made of rhenium during the irradiations. Hence, besides the experimental determination of the photoneutron reaction yield of the  $^{142}\text{Ce}(\gamma, n)$  reaction, the reaction yield for the  $^{187}\text{Re}(\gamma, n)$  reaction can be determined experimentally using Eq. (1).

The cross section of the  $^{187}\text{Re}(\gamma, n)$  reaction was studied previously in detail (see Ref. [23]). The following parametrization of the cross section was used in the data analysis:

for  $S_n < E \leq 8.55$  MeV:

$$\sigma(E) = (80.4 \pm 9.6) \text{mb} \sqrt{\frac{E - S_n}{S_n}}; \quad (8)$$

for  $8.55$  MeV  $< E \leq 9.50$  MeV:

$$\begin{aligned} \frac{\sigma(E)}{\text{mb}} = & -17 \left( \frac{E}{\text{MeV}} \right)^3 + 4.7 \times 10^2 \left( \frac{E}{\text{MeV}} \right)^2 \\ & - 4.3 \times 10^3 \left( \frac{E}{\text{MeV}} \right) + 1.3 \times 10^4; \end{aligned} \quad (9)$$

and for  $9.50$  MeV  $< E \leq 19.00$  MeV:

$$\begin{aligned} \sigma(E) = & \frac{250 \text{mb}(2.83 \text{ MeV} E)^2}{(E^2 - 158.76 \text{ MeV}^2)^2 + (2.83 \text{ MeV} E)^2} \\ & + \frac{296 \text{mb}(5.30 \text{ MeV} E)^2}{(E^2 - 243.36 \text{ MeV}^2)^2 + (5.30 \text{ MeV} E)^2}. \end{aligned} \quad (10)$$

Equation (8) stems from the experiments described in Ref. [23], and Eq. (10) is a fit to the giant dipole resonance presented in Ref. [33]. Equation (9) is also derived in Ref. [23] to allow for a continuous link function between Eqs. (8) and (10).

Inserting this cross section into Eq. (6) and using the spectral distribution of the photon flux obtained via the procedure described in Sec. IIIA, the absolute value of the photon flux can be determined. This absolute value of the photon flux is then used for the data analysis of the cerium targets. In order to extract a cross section for the  $^{142}\text{Ce}(\gamma, n)$  reaction, a constant cross section for the respective energy range was assumed as

TABLE III. Experimental cross-section results for the  $^{142}\text{Ce}(\gamma, n)$  reaction. The photon energy  $E_\gamma$  corresponds to the energy where the photon flux of the fit function is a maximum. The FWHM of the fit function is stated as well.

$E_\gamma$ (keV)	FWHM (keV)	$\sigma_0$ (mb)
$7640^{+103}_{-191}$	294	$10.21 \pm 2.40$
$8149^{+117}_{-205}$	322	$22.08 \pm 4.64$
$8465^{+121}_{-239}$	360	$20.10 \pm 4.33$
$8758^{+130}_{-243}$	373	$25.32 \pm 4.60$
$9102^{+128}_{-238}$	366	$30.16 \pm 5.45$
$9315^{+133}_{-283}$	416	$29.82 \pm 4.93$
$9669^{+141}_{-300}$	441	$39.32 \pm 6.98$

a first-order approximation,

$$\sigma_0 = \frac{Y(E_\gamma)}{I_\gamma(E_\gamma)\varepsilon(E_\gamma)\tau N_{\text{target}} \int_0^\infty N_\gamma(E)dE}. \quad (11)$$

Due to the fact that the FWHM of the HI $\gamma$ S beam is much smaller than nonlinear changes in the cross section, a more complex procedure as described in Ref. [34] is not necessary [35].

#### IV. RESULTS AND DISCUSSION

The experimental data of the photoneutron reaction on  $^{142}\text{Ce}$  have been analyzed to determine cross-section data as described in the preceding section. The results are summarized in Table III and presented in Fig. 2 as a function of the excitation energy. The quoted photon energy  $E_\gamma$  corresponds to the value of the energy where the photon flux has its maximum. The cross-section results are averaged values for the energy ranges covered by the laser Compton backscattered spectra.

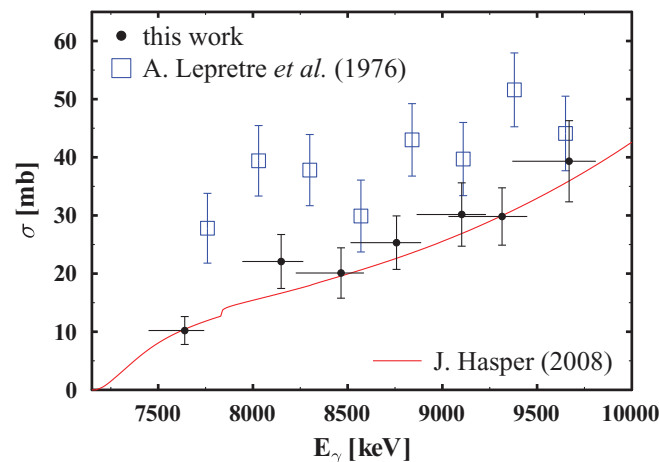


FIG. 2. (Color online) Experimentally determined cross-section results for the reaction  $^{142}\text{Ce}(\gamma, n)$  are depicted as a function of photon energy.

In Fig. 2 the derived cross-section data are compared to experimental data from measurements using the positron-annihilation in-flight technique [36]. Our experimental cross-section results are systematically smaller than the ones of A. Lepretre *et al.* However, the experimental results of the Saclay group are systematically higher compared to other experiments as observed for various reactions [37].

Recently, the  $^{142}\text{Ce}(\gamma, n)$  reaction was measured using bremsstrahlung at the Darmstadt High-Intensity Photon Setup [38] at the superconducting Darmstadt linear accelerator as well [39]. According to the analysis described in Ref. [39], normalization factors have been derived for the predicted photoneutron cross section using the statistical-model codes NON-SMOKER<sup>WEB</sup> [40] and TALYS [41,42]. In the case of the NON-SMOKER<sup>WEB</sup> code, a normalization factor of 1.02 was derived, i.e., an excellent description of the bremsstrahlung data. The normalized prediction of the NON-SMOKER<sup>WEB</sup> code is also shown in Fig. 2. As can be seen, these results are in excellent agreement with our experimental cross-section data.

Our experimental results are also compared to theoretical predictions calculated with the recent version of the TALYS code [41,43]. The sensitivity of the model calculation to the neutron optical model potential and the nuclear level density within the TALYS code with all available inputs was investigated. Insensitivity to these two quantities was observed. Thus, the cross-section predictions are exclusively sensitive to the  $\gamma$ -ray strength function in the measured energy range. Therefore, the code was used with its default settings and only the  $\gamma$ -ray strength function was varied. The theoretical predictions are depicted in Fig. 3 together with the new experimental data. In total, five different  $\gamma$ -ray strength functions were used: standard Lorentzian [44], microscopic Hartree-Fock BCS [45], microscopic Hartree-Fock-Bogoliubov [46], microscopic

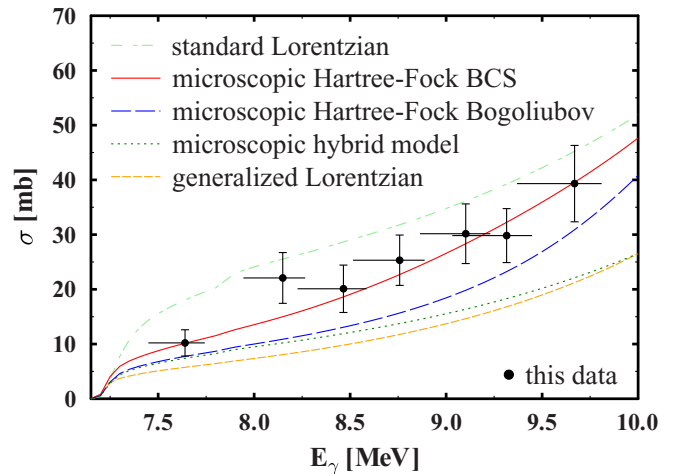


FIG. 3. (Color online) The experimentally determined cross-section data of the reaction  $^{142}\text{Ce}(\gamma, n)$  are compared with statistical-model calculations using the TALYS code [41,43]. The calculations were performed using the default settings, but the  $\gamma$ -ray strength function was varied. In total, five  $\gamma$ -ray strength functions were used: standard Lorentzian [44], microscopic Hartree-Fock BCS [45], microscopic Hartree-Fock-Bogoliubov [46], microscopic hybrid model [47], and generalized Lorentzian [48].

hybrid model [47], and generalized Lorentzian [48]. The experimental results are well reproduced by the calculation using a microscopic description within the framework of the Hartree-Fock-BCS model. Since the inverse reaction takes place in the  $s$  process, the Maxwellian averaged cross section (MACS) at  $kT = 30$  keV for the  $^{141}\text{Ce}(n,\gamma)^{142}\text{Ce}$  reaction was calculated using the same  $\gamma$ -ray strength function as input of the TALYS code:  $\langle\sigma\rangle_{30\text{keV}} = 59$  mb. The value for 30 keV agrees within the large uncertainties with the recommended value of  $\langle\sigma\rangle_{30\text{keV}}^{\text{Kadonis}} = 76 \pm 33$  mb [49] but is about a factor of 1.3 smaller. Using this significantly reduced MACS in the  $s$ -process network calculation NETZ [50,51] yields a reduction of the  $^{142}\text{Ce}$  abundance by 20% compared to the result using the standard value given of Kadonis. This can easily be understood since the  $s$ -process flow is redirected towards the  $\beta$  decay branch of  $^{141}\text{Pr}$ . Consequently, the amount of  $^{141}\text{Pr}$  produced with the smaller MACS is enlarged by 6%. This might yield interesting consequences in more detailed  $s$ -process studies since  $^{141}\text{Pr}$  is part of the second  $s$ -process peak.

## V. SUMMARY AND CONCLUSION

We have measured the cross section of the  $^{142}\text{Ce}(\gamma,n)$  reaction just above the reaction threshold. The cross-section results are compared to predictions within the statistical model using the code TALYS. These calculations apply different models

for the  $\gamma$ -ray strength function. A very good reproduction of the experimental data is obtained using the TALYS code in combination with the  $\gamma$ -ray strength function of Ref. [45]. Using this  $\gamma$ -ray strength function to calculate the MACS at  $kT = 30$  keV for the inverse reaction  $^{141}\text{Ce}(n,\gamma)$  yields an enhanced production of  $^{141}\text{Pr}$  by 6% in the  $s$ -process network calculation NETZ [50,51]. Concerning  $p$ -process nucleosynthesis, our experimental results for the reaction  $^{142}\text{Ce}(\gamma,n)$  agrees with the TALYS calculation using the  $\gamma$ -ray strength function of Ref. [45]. This proves that the assumptions of the model, such as the high level density, are fulfilled even though a closed neutron-shell is approached. Besides, the result is an important step to provide a more complete database of photon-induced reactions in the mass region  $A \geq 140$  covered by the  $\gamma$  process.

## ACKNOWLEDGMENTS

The authors acknowledge the help of the accelerator staff at DFELL. Furthermore, we thank Michael Reese for his help with the program matfit. This project has been supported by the Deutsche Forschungsgemeinschaft under Contract Nos. SFB 634 and SO907/2-1, by the Alliance Program of the Helmholtz Association (HA216/Emmi), by the HIC for FAIR within the framework of LOEWE launched by the State of Hesse, Germany, as well as by the US Department of Energy, Office of Nuclear Physics, under Grant No. DE-FG02-97ER41003.

- 
- [1] F. Käppeler, R. Gallino, S. Bisterzo, and W. Aoki, *Rev. Mod. Phys.* **83**, 157 (2011).
- [2] R. Gallino, C. Arlandini, M. Busso, M. Lugaro, C. Travaglio, O. Straniero, A. Chieffi, and M. Limongi, *Astrophys. J.* **497**, 388 (1998).
- [3] M. Arnould, S. Goriely, and K. Takahashi, *Phys. Rep.* **450**, 97 (2007).
- [4] J. J. Cowan, F. K. Thielemann, and J. W. Truran, *Phys. Rep.* **208**, 267 (1991).
- [5] M. Arnould and S. Goriely, *Phys. Rep.* **384**, 1 (2003).
- [6] T. Rauscher, N. Dauphas, I. Dillmann, C. Fröhlich, Zs. Fülöp, and Gy. Gyürky, *Rep. Prog. Phys.* **76**, 066201 (2013).
- [7] S. E. Woosley and W. M. Howard, *Astrophys. J. Suppl.* **36**, 285 (1978).
- [8] M. Rayet, M. Arnould, M. Hashimoto, N. Prantzos, and K. Nomoto, *Astron. Astrophys.* **298**, 517 (1995).
- [9] W. Hauser and H. Feshbach, *Phys. Rev.* **87**, 366 (1952).
- [10] T. Rauscher and F.-K. Thielemann, *At. Data Nucl. Data Tables* **75**, 1 (2000).
- [11] K. Vogt, P. Mohr, M. Babilon, W. Bayer, D. Galaviz, T. Hartmann, C. Hutter, T. Rauscher, K. Sonnabend, S. Volz, and A. Zilges, *Nucl. Phys. A* **707**, 241 (2002).
- [12] K. Sonnabend, P. Mohr, K. Vogt, A. Zilges, T. Rauscher, H. Beer, F. Käppeler, and R. Gallino, *Astrophys. J.* **583**, 506 (2003).
- [13] K. Sonnabend, K. Vogt, D. Galaviz, S. Müller, and A. Zilges, *Phys. Rev. C* **70**, 035802 (2004).
- [14] S. Goko, H. Utsunomiya, S. Goriely, A. Makinaga, T. Kaihori, S. Hohara, H. Akimune, T. Yamagata, Y.-W. Lui, H. Toyokawa, A. J. Koning, and S. Hilaire, *Phys. Rev. Lett.* **96**, 192501 (2006).
- [15] J. Hasper, S. Müller, D. Savran, L. Schnorrenberger, K. Sonnabend, and A. Zilges, *Phys. Rev. C* **77**, 015803 (2008).
- [16] C. Nair, M. Erhard, A. R. Junghans, D. Bemmerer, R. Beyer, E. Grosse, J. Klug, K. Kosev, G. Rusev, K. D. Schilling, R. Schwengner, and A. Wagner, *Phys. Rev. C* **78**, 055802 (2008).
- [17] H. Utsunomiya, S. Goriely, T. Kondo, T. Kaihori, A. Makinaga, S. Goko, H. Akimune, T. Yamagata, H. Toyokawa, T. Matsumoto, H. Harano, S. Hohara, Y.-W. Lui, S. Hilaire, S. Péru, and A. J. Koning, *Phys. Rev. Lett.* **100**, 162502 (2008).
- [18] J. Hasper, D. Galaviz, S. Müller, A. Sauerwein, D. Savran, L. Schnorrenberger, K. Sonnabend, and A. Zilges, *Phys. Rev. C* **79**, 055807 (2009).
- [19] S. Müller, Ph.D. thesis, Technische Universität Darmstadt, 2009.
- [20] O. Ershova, P. Adrich, H. Alvarez-Pol, F. Aksouh, T. Aumann, M. Babilon, K.-H. Behr, J. Benlliure, T. Berg, M. Böhmer, K. Boretzky, A. Brünle, R. Beyer, E. Casarejos, M. Chartier, A. Chatillon, D. Cortina-Gil, U. Datta Pramanik, L. Deveaux, M. Elvers, T. W. Elze, H. Emling, M. Erhard, B. Fernandez-Dominguez, H. Geissel, M. Gorska, M. Heil, M. Hellström, G. Ickert, H. Johansson, A. R. Junghans, F. Käppeler, O. Kisilev, A. Klimkiewicz, J. V. Kratz, R. Kulessa, N. Kurz, M. Labiche, T. Le Bleis, R. Lemmon, K. Lindenberg, Y. Litvinov, P. Maierbeck, A. Movsesyan, S. Müller, T. Nilsson, C. Nociforo, N. Paar, R. Palit, S. Paschalis, R. Plag, W. Prokopowicz, R. Reifarth, D. Rossi, L. Schnorrenberger, H. Simon, K. Sümmerner, G. Surowka, D. Vretenar, A. Wagner, S. Walter, W. Walus, H. Weick, N. Winckler, M. Winkler, and A. Zilges, in *Proceedings of the 11<sup>th</sup> Symposium on Nuclei in the Cosmos, PoS. (NIC XI) 232, Heidelberg, Germany, July 19–23, 2010*, edited by

- K. Blaum, N. Christlieb, and G. Martinez-Pinedo (SISSA, <http://pos.sissa.it/cgi-bin/reader/conf.cgi?confid=100>, 2010).
- [21] R. Raut, A. P. Tonchev, G. Rusev, W. Tornow, C. Iliadis, M. Lugaro, J. Buntain, S. Goriely, J. H. Kelley, R. Schwengner, A. Banu, and N. Tsoneva, *Phys. Rev. Lett.* **111**, 112501 (2013).
- [22] T. Rauscher, *Astrophys. J. Suppl.* **201**, 26 (2012).
- [23] S. Müller, A. Kretschmer, K. Sonnabend, A. Zilges, and D. Galaviz, *Phys. Rev. C* **73**, 025804 (2006).
- [24] H. R. Weller, W. Ahmed, H. Gao, W. Tornow, Z. K. Wu, M. Gai, and R. Miskimen, *Prog. Part. Nucl. Phys.* **62**, 257 (2009).
- [25] M. Scheck, V. Yu. Ponomarev, T. Aumann, J. Beller, M. Fritzsche, J. Isaak, J. H. Kelley, E. Kwan, N. Pietralla, R. Raut, C. Romig, G. Rusev, D. Savran, K. Sonnabend, A. P. Tonchev, W. Tornow, H. R. Weller, and M. Zweidinger, *Phys. Rev. C* **87**, 051304(R) (2013).
- [26] C. Romig, J. Beller, J. Glorius, J. Isaak, J. H. Kelley, E. Kwan, N. Pietralla, V. Yu. Ponomarev, A. Sauerwein, D. Savran, M. Scheck, L. Schnorrenberger, K. Sonnabend, A. P. Tonchev, W. Tornow, H. R. Weller, A. Zilges, and M. Zweidinger, *Phys. Rev. C* **88**, 044331 (2013).
- [27] P. De Bièvre and P. D. P. Taylor, *Int. J. Mass Spectrom. Ion Phys.* **123**, 149 (1993).
- [28] G. Audi, M. Wang, A. H. Waspra, F. G. Kondev, M. MacCormick, X. Xu, and B. Pfeiffer, *Chinese Physics C* **36**, 1287 (2012).
- [29] National Nuclear Data Center, <http://www.nndc.bnl.gov/ensdf>.
- [30] S. Agostinelli *et al.*, *Nucl. Instrum. Methods A* **506**, 250 (2003).
- [31] D. J. G. Love and A. H. Nelson, *Nucl. Instrum. Methods A* **274**, 541 (1989).
- [32] C. Sun, Y. K. Wu, G. Rusev, and A. Tonchev, *Nucl. Instrum. Methods A* **605**, 312 (2009).
- [33] A. M. Goryachev, G. N. Zalesnyie, S. F. Semenko, and B. A. Tulupov, *Yad. Fiz.* **17**, 463 (1973).
- [34] H. Utsunomiya, A. Makinaga, S. Goko, T. Kaihori, H. Akimune, T. Yamagata, M. Ohta, H. Toyokawa, S. Müller, Y.-W. Lui, and S. Goriely, *Phys. Rev. C* **74**, 025806 (2006).
- [35] A. P. Tonchev, S. L. Hammond, C. R. Howell, C. Huibregste, A. Hutcheson, J. H. Kelley, E. Kwan, R. Raut, G. Rusev, W. Tornow, T. Kawano, D. J. Vieira, and J. B. Wilhelmy, *Phys. Rev. C* **82**, 054620 (2010).
- [36] A. Lepretre, H. Beil, R. Bergere, P. Carlos, J. Fagot, A. de Miniac, and A. Miyase, *Nucl. Phys. A* **258**, 350 (1976).
- [37] B. L. Berman, R. E. Pywell, S. S. Dietrich, M. N. Thompson, K. G. McNeill, and J. W. Jury, *Phys. Rev. C* **36**, 1286 (1987).
- [38] K. Sonnabend, D. Savran, J. Beller, M. A. Büssing, A. Constantinescu, M. Elvers, J. Endres, M. Fritzsche, J. Glorius, J. Hasper, J. Isaak, B. Löher, S. Müller, N. Pietralla, C. Romig, A. Sauerwein, L. Schnorrenberger, C. Wälzlein, A. Zilges, and M. Zweidinger, *Nucl. Instrum. Methods A* **640**, 6 (2011).
- [39] J. Hasper, Ph.D. thesis, Technische Universität Darmstadt, 2008.
- [40] NON-SMOKER<sup>WEB</sup> version 4.6.0, <http://nucastro.org/nonsmoker.html>.
- [41] A. J. Koning, S. Hilaire, and M. C. Duijvestijn, in *Proceedings of the International Conference on Nuclear Data for Science and Technology-ND2007, April 22–27, 2007, Nice, France*, edited by O. Bersillon, F. Gunsing, E. Bauge, R. Jacqmin, and S. Leray (EDP Sciences, Paris, 2008), pp. 211–214.
- [42] TALYS-1.0, <http://www.talys.eu>.
- [43] TALYS-1.4, <http://www.talys.eu>.
- [44] J. Kopecky and M. Uhl, *Phys. Rev. C* **41**, 1941 (1990).
- [45] S. Goriely and E. Khan, *Nucl. Phys. A* **706**, 217 (2002).
- [46] S. Goriely, E. Khan, and M. Samyn, *Nucl. Phys. A* **739**, 331 (2004).
- [47] S. Goriely, *Phys. Lett. B* **436**, 10 (1998).
- [48] D. M. Brink, *Nucl. Phys.* **4**, 215 (1957); P. Axel, *Phys. Rev.* **126**, 671 (1962).
- [49] I. Dillmann, R. Plag, F. Käppeler, and T. Rauscher in *Proceedings of the Scientific Workshop on Neutron Measurements, Theory and Applications Nuclear data for Sustainable Nuclear Energy, 28-30 April, 2009, Geel, Belgium*, edited by F.-J. Hamsch, p. 55 (2010), <http://papercc.de/11411-efnudat-fast-neutrons-9789279117053#!/pages/55>.
- [50] S. Jaag, NETZ, Internal Report 14.01, 01, /P35G. Forschungszentrum Karlsruhe (1991).
- [51] R. Reifarh, F. Käppeler, F. Voss, K. Wisshak, R. Gallino, M. Pignatari, and O. Straniero, *Astrophys. J.* **614**, 363 (2004).